Chemical reactions in H2O:CO interstellar ice analogs promoted by energetic heavy ion irradiation

A de Barros, C Mejía, E Seperuelo Duarte, Alicja Domaracka, P Boduch, H Rothard, E da Silveira

Preprint 10 December 2021

Chemical reactions in H_2O:CO interstellar ice analogs promoted by energetic heavy ion irradiation

A. L. F. de Barros[1], C. Mejía[2], E. Seperuelo Duarte[3], A. Domaracka[4], P. Boduch[4], H. Rothard[4], E. F. da Silveira[5]

[1] *Departamento de Física, Centro Federal de Educação Tecnológica Celso Suckow da Fonseca, Av. Maracanã 229, 20271-110 Rio de Janeiro, RJ, Brazil*

[2] *Facultad de Ciencias Químicas, Universidad de Cuenca, Av. 12 de Abril y Loja, 010202, Cuenca, Ecuador*

[3] *Instituto Federal de Educação, Ciência e Tecnologia, Rio de Janeiro, RJ, Brazil*

[4] *Centre de Recherche sur les Ions, les Matériaux et la Photonique Normandie Univ, ENSICAEN, UNICAEN, CEA, CNRS, CIMAP, 14000 Caen, France*

[5] *Departamento de Física, Pontifícia Universidade Católica do Rio de Janeiro, Rua Marquês de São Vicente 225, 22451-900, Rio de Janeiro, RJ, Brazil*

Received

ABSTRACT

H_2O:CO, at concentrations of (3:2) and (10:1), was condensed on CsI substrate at 15 K and irradiated with 46 MeV $^{58}Ni^{11+}$ ion beam. Radiolysis induced by fast heavy ions was analyzed by infrared spectroscopy (FTIR). The formation of nine molecular species, CO_2, H_2O_2, HCOOH, HCO, H_2CO, $^{13}CO_2$, CH_3OH, O_3 and C_3O_2 was observed. For both concentrations, carbon dioxide (CO_2), formaldehyde (H_2CO), formic acid (HCOOH), and hydrogen peroxide (H_2O_2) are the most abundant products species, and tricarbon dioxide (C_3O_2) is much less abundant. Precursor destruction cross sections and formation cross sections of products are determined. The CO destruction cross section for the (3:2) concentration is almost five times higher than that of water, while those for the (10:1) concentration are practically the same. Atomic sputtering yields are estimated for the two ice films, the total mass sputtered is approximately 2.5×10^6 u per impact. These results contribute to figure out the chemical pathways of compounds synthesized from the two most abundant organic species (H_2O and CO) observed in the ices of grain mantles of the circumstellar envelopes and interstellar medium. In additional, the finding results reveal that molecular astronomical percentages are comparable to those obtained after 15 eV molec^{-1} of deposited dose in current experiments compared with the relative concentration of molecules in solid phase observed in MYSO, LYSO, BG Stars, and Comets.

Key words: astrochemistry – methods: laboratory:solid state – astronomical instrumentation, methods and techniques, FTIR – Cosmic rays – interstellar Medium (ISM) – Trans Neptunian Objects.

1 INTRODUCTION

The low temperatures of denses circumstellar envelopes and of the interstellar medium (ISM) are necessary conditions for forming mantles of condensed molecules over silicate and carbonaceous dust grains. At these regions, abundant H_2O is easily observed mixed with CO, CO_2, CH_3OH, NH_3 molecules, CO being the second most abundant one (Öberg et al. 2011; Tielens et al. 2013; Boogert et al. 2015). These molecules are also found in comets (Mumma & Charnley 2011). The evolution of ices rich in organic compounds could largely be correlated to ionizing radiation such as UV-photons, electrons, light and heavy ions (Bennett et al. 2013).

Duley (1974) reported the existence of solid CO bands in the infrared spectra (IR) of cold regions grain mantles. Soifer et al. (1979) observed weak absorption features at 4.61 μm (solid CO) and 4.67 μm (gaseous CO) in the infrared source W33 A. Unfortunately, due to low resolution of the data, the quantity of CO was undetermined.

Solid CO, particularly dissolved in H_2O ice, has been found in many regions of our Galaxy (Soifer et al. 1979). Lacy et al. (1984) used a high-resolution spectrometer to observe the 4.61 μm (2140 cm^{-1}) infrared band and confirm the existence of solid CO in the interstellar grains located inside the dense clouds W33A and NGC 7538 IRS9. Larson (1985) also detected CO ice in the dense clouds of the massive stellar object W33A. (Soifer et al. 1979) and Shuping et al. (2000) have been identified solid CO infrared bands in the quiescent dense clouds and their cores in different regions such as intermediate, low, and massive stellar objets (namely, IMYSO, LMYSO, MYSO respectively), galactic centre (GC), comets and the solar system. Kerr et al. (1993) observed solid CO in the ρ Ophiuchi molecular cloud and Shuping et al. (2000) calculated the percentage of CO/H_2O abundance ratio as 5 – 36%. Solid CO has been found in the embedded and background sources of Taurus dark cloud with a CO/H_2O ~ 30% by Chiar et al. (1995). Whittet et al. (2009) analyzed the infrared spectrum behind a dark filament in the Cocoon Nebula (IC 5146) and claimed that solid CO coexists in an ice containing about 85% of apolar environment and with a percentage

from 2 −8% of H_2O. Further observations found CO/H_2O abundance of 15 − 40% of H_2O (Whittet et al. (2007); Chiar et al. (2011); Whittet et al. (2013); Boogert et al. (2013); Noble et al. (2013), and references therein).

In the MYSO envelopes, solid CO was found by Geballe (1986) towards several obscured infrared objects, and Gibb et al. (2004) calculated the CO/H_2O as < 12 in Sgr A*, < 31% in GCS 3I and < 30% in GCS 4 with respect to H_2O abundances in the IR sources of these diffuse and dense regions of the ISM located in the GC. Ices containing CO and H_2O in the IR sources of MYSO of Magellanic Clouds were observed by Shimonishi et al. (2010) in the embedded YSO, Oliveira et al. (2011) in the large and small clouds Magellanic Clouds (LMC and SMC), and by Pauly et al. (2018) in the envelopes of YSO. They estimated a solid CO percentages of 2 − 14% H_2O in the LMC and a 0.5 − 3% H_2O in the SMC.

CO ice mixtures have been found embedded in the star-forming environments LMYSO by Pontoppidan et al. (2003), with 8 − 52% of CO/H_2O (Pontoppidan et al. 2008). Thi et al. (2006) observed, from IR soures, 4 − 55% CO/H_2O in the envelope around IMYSO of the Southern Vela molecular cloud. In the circumstellar disk CRBR 2422.8 − 3423, in Ophiuchus around LMYSO, solid CO was reported by Pontoppidan et al. (2005) and Aikawa et al. (2012) who detected a percentage of 13 − 90% H_2O in the circumstellar disks and envelopes of LMYSO towards the class 0−I sources L1527, IRC−L1041−2, and IRAS 04302.

IR features of ices containing CO and H_2O were observed in the GC regions: Rho Ophiuchus source, and WL16 by McFadzean et al. (1989), Sagittarius A* and GCS 3 by Moneti et al. (2011), Sagittarius A* by Chiar et al. (2002), and central stellar cluster of the Milky Way by Moultaka et al. (2009). Additionally, CO and H_2O ices were observed by Spoon et al. (2000) in the central region close to the starburst galaxy NGC 4945, and Spoon et al. (2004) observed solid CO in the galaxy IRAS F001837111. In comets, the observations of CO and H_2O ice mixtures have been summarized by Mumma & Charnley (2011) (see references therein), where the percentage of CO with respect to H_2O varies from 4 to 30%.

In astronomical and experimental observations of solid $CO:H_2O$ ices, the CO stretch mode appears in three main components: the blue one at 2143 cm^{-1}, a middle one at 2140 cm^{-1}, and the red one at 2134 cm^{-1} (Pontoppidan et al. 2003). Those IR components depend on their physical environment: the red component corresponds to CO interacting with polar molecules (i.e., H_20, NH_3), while the middle component is caused by its interaction with apolar molecules (i.e., N_2, O_2, CO_2, or CO itself) (Gibb et al. 2004). The variations of the band 2140 cm^{-1} are attributed to **distinct** chemical compositions and/or physical properties of the matrix ice. The narrow 2140 cm^{-1} feature is generated by CO trapped in apolar ices, while the broad feature is characteristic of CO trapped in polar ices, such as H_20 ice (Tielens et al. 1991; Chiar et al. 1995). Recently, the CO stretch mode band has been decomposed in six components (Seperuelo Duarte et al. 2021). Each component is attributed to the interaction between CO and different sites in the ice.

In laboratory, $CO:H_2O$ ice analogues have been exposed to ionizing irradiation to simulate cosmic irradiation of grain mantle existing in dense clouds. $CO:H_2O$ photolysis by UV has demonstrated that new species such as HCO, H_2CO, CH_3OH, CO_2, and HCOOH are produced (Allamandola et al. 1988; Schutte et al. 1999; Watanabe et al. 2007). The X-ray irradiation of $CO:H_2O$ ices synthesizes CH_4, HCO, H_2CO, CH_3OH, H_2O_2, C_3, C_2O, CO_2, and $HCOO^-$, HOCO, HCOOH, CO_3 and C_3O_2 (Jiménez-Escobar, et al. 2016). Munoz et al. (2019), analyzing the UV with X-ray photolysis in $CO:H_2O$ ices, found similar physical-chemical changes and photoproducts. The HCOOH production from $CO:H_2O$ mixture dissolved into a frozen noble gas matrix irradiated by X-rays was studied by Ryazantsev et al. (2020); they concluded that the formed radicals react to synthesize HCOOH when the ice matrix is warmed up. Bennett et al. (2010) used **5keV** electrons to irradiate $CO:H_2O$, synthesizing HCO, H_2CO, CO_2, HOCO and HCOOH, with no evidence of H_2O_2. Hudson & Moore (1999) irradiated $CO:H_2O$ ice with protons (0.8 MeV) and identified the products: CH_4, HCO, H_2CO, CO_2, HCOOH, and CH_3OH. Similar results were obtained by Hudson & Moore (2001); Ioppolo et al. (2009); Suhasaria et al. (2017). It is important to mention that Watanabe et al. (2007) irradiated $CO:H_2O$ ice with both UV photons and protons, simultaneously, to simulate more realistic cosmic irradiation of ices. Their results reveal similar chemical changes produced by UV and protons.

In the current work, we use heavy ions to simulate the physical-chemical changes triggered by heavy cosmic ray irradiation on ices that recover grain mantles, particularly those located in the coolest ISM regions, that is, in the interior of dense clouds. This study fills a gap in the research on the effects of energetic heavy ions in mixtures of $CO:H_2O$ ices. The formed **species** in our experiments are: CO_2, H_2O_2, HCOOH, HCO, H_2CO, $^{13}CO_2$, CH_3OH, O_3, $HCOO^-$, HOCO and C_3O_2. Two different $CO:H_2O$ concentrations have been analyzed to permit interpolation. Cross-sections and sputtering yields are also determined.

2 EXPERIMENTAL SETUP

The experiments were carried out inside a high vacuum chamber (10^{-8} mbar at 15 K) at the IRRadiation SUD (IRRSUD) beamline of the French National Heavy Ion Accelerator (GANIL), using the CASIMIR set-up of CIMAP-CIRIL ("Centre de recherche sur les Ions, Matériaux et la Photonique") details at Seperuelo Duarte et al. (2009); de Barros et al. (2011). Briefly, a closed-cycle helium cryostat finger is in thermal contact with a sample holder containing a clean CsI substrate disk, that was kept for 6 h inside the vacuum chamber at 10^{-8} mbar. The heater system allows to increase the temperature with selectable ramps up to 300 K. Initially a "blank experiment—type" has been performed with the same system and without gas deposition (details at Mejía et al. (2013)). The gas mixing of H_2O:CO (at pressure 4 mbar) was injected onto a cold IR transparent window, CsI substrate, placed 10 mm away, via a 4 mm diameter thin tube connected to the irradiation chamber, at a base pressure of 10^{-6} mbar. An ultra pure liquid water with an

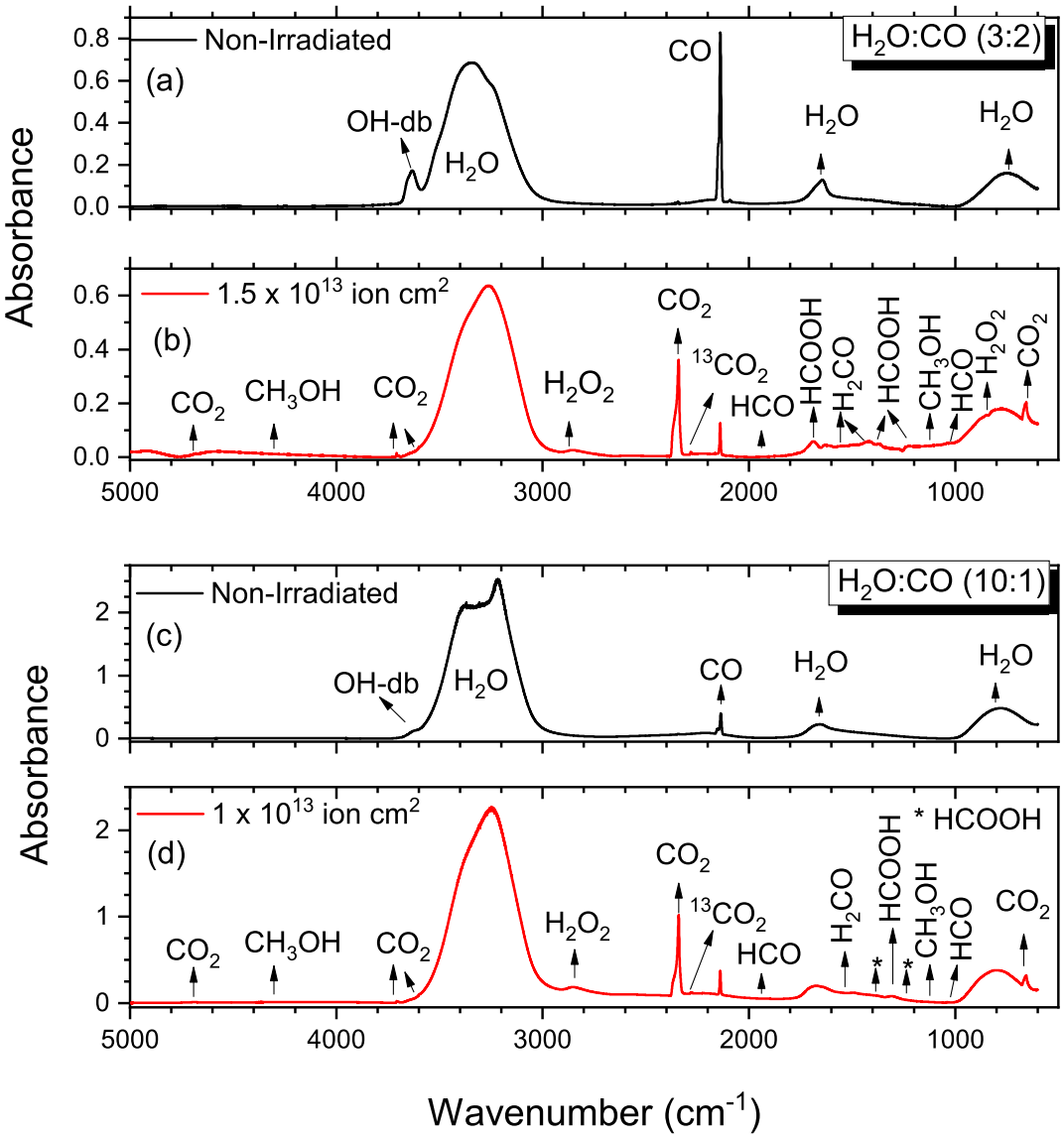

Figure 1. (a) and (c) Mid-IR spectra of the non-irradiated H_2O:CO (3:2) and (10:1) mixture ices at 15 K, respectively. The H_2O and CO main bands, with their wavenumber positions, are pointed out in the top of the figures (b) and (d). The same spectral region but at 1.5×10^{13} fluence for (3:2) and at 1×10^{13} fluence for (1:10) concentrations.

electric conductivity of 10^7 Ω cm (Milli-Q) was evaporated at low pressure and mixed with CO gas, whose purity was 99.99% purity (Messer Griesheim).

After 5 min, a valve was opened to inject the gas mixture in the chamber and deposit it onto the substrate for nearly 3 and 2 minutes for the (3:2) ice and for the (10:1) ice, respectively. During the gas deposition, the pressure in the main chamber rose up to 10^{-7} mbar. The deposition rate was about 10 ± 2 nm s^{-1}, kept constant up to the ice layers attain the thicknesses of the 3.4 μm and 2.1 μm of the (3:2) and (10:1) ice layers, respectively. FTIR analysis showed that H_2O molecules from the residual gas became stuck over the two sides of the CsI substrate with a rate of 8×10^{14} molec h^{-1} cm^{-2}. The condensation of these gases at this deposition rate produced a porous and amorphous ice mixture; this was verified by infrared absorption (Mejía et al. 2015a). Assuming the same condensation rate, less than 2.5×10^{15} molec h^{-1} cm^{-2} of H_2O would condense over the substrate during the same time of the irradiation experiment.

The reason to use $^{58}Ni^{+13}$ ion beam is because iron and nickel are relatively abundant heavy ion cosmic-ray components, roughly

Table 1. H_2O and CO precursor bands used for the cross section calculations. Band positions, integration limits, vibration modes and assignments, molar mass (M) in g mol^{-1}, mass density (ρ) in g cm^{-3} and literature A-values (A_v) in $\times$ 10^{-17} cm molec^{-1}, initial (N_0) and final (N_f) column densities in 10 ^{18} molec cm^{-2} for the precursors.

Molecule	Position cm^{-1}	Position μm	Integration limits cm^{-1}	Mode	M g mol^{-1}	ρ g cm^{-3}	A_v cm molec^{-1}	N_0 (3:2)	N_f (3:2)	N_0 (10:1)	N_f (10:1)
H_2O	760	12.4	1005.3 - 611.3	ν_L O-H libration	28	0.81 [a]	3.1[b]	2.7	1.7	9.1	6.3
CO	2138	4.68	2147.4 - 2122.1	ν_1 ^{12}C≡O stretch	18	0.94 [c]	1.1[b,d]	2.1	0.17	0.87	0.39

[a] Loeffler & Baragiola (2005), [b] Gerakines et al. (1994), [c] Hama and Watanabe (2013), [d] Jamieson et al. (2006).

2.2×10^{-4} with respect to protons (Tanabashi et al. 2018). The average radiolysis effects of heavy ions can be as far as 10^3 times higher than those of protons at the same velocity and with the same flux (de Barros et al. 2011; Mejía et al. 2013). The Ni bombardment was performed at normal incidence on the H_2O:CO ice films. The exposure to swift heavy ion bombardment lasted 170 minutes long for both samples. The energy rate transferred per projectile via electronic interaction is around S_e = 1578 $\times$ 10^{-15} eV molec^{-1} cm^{-2} for the (3:2) concentration and S_e = 1486 $\times$ 10^{-15} eV molec^{-1} cm^{-2} for the (10:1) concentration, values obtained by SRIM code (Ziegler et al. 2010). **The 46 MeV $^{58}Ni^{13+}$ ion projectiles flux was $\sim 1 \times 10^9$ cm^{-2}s^{-1} at fluences of 0.01, 0.05, 0.1, 0.5, 1.0, 2.5, 5.0, 7.5 and 10 $\times$ 10^{12} ion cm^{-2}, for (10:1) and at final fluence of 15 $\times$ 10 ^{12} ion cm^{-2} for (3:2), where after each irradiation the FTIR spectrum was acquired.** The range of these projectiles is 20 μm, large enough to traverse completely the 3.4 μm and 2.1 μm ice thick of the (3:2) and (10:1) ice layers, respectively.

The ice sample was probed by a Nicolet Magna 550 Fourier Transform Infrared Spectrometer running in transmission mode, with the beam impinging perpendicularly to the surface of the sample surface. Each IR spectrum was acquired by 256 scans in the 5000 – 600 cm^{-1} (2 – 16.7 μm) region, at 4 cm^{-1} of resolution.

3 RESULTS

The H_2O:CO condensation at this deposition rate produces a porous amorphous ice mixture. This amorphous structure can be verified by the existence of water band absorption of the water dangling molecules in pores surfaces at the 3626 cm^{-1} wavenumber (Mejía et al. 2015b). Figs. 1a and 1c show the observed IR spectra of the one non-irradiated H_2O + CO ice mixtures; Figs. 1b and 1d present the spectra of the irradiated samples at 1 $\times$ 10^{13} ions cm^{-2} fluence, for the H_2O:CO (3:2) and (10:1) concentrations, respectively.

3.1 Compaction of porous ice mixture

The structure of the mixed ice reveals a certain degree of porosity observed in the absorptions of the so-called dangling bond (db-OH) of the water, which is located at 3636 cm^{-1} for the CO:H_2O mixture ices. Figure 1 shows the db-OH in the non-irradiated ice mixture, whereas Figures 2 and 3 present the gradual disappearance of this feature until the fluence of 10^{12} ions cm^{-2}, when the ice mixture becomes amorphous and compacted with minimum porosity (Mejía et al. 2015a).

At the beginning of irradiation (F < 10^{12} ions cm^{-2}), corresponding to doses relatively small (< 1.5 eV molec^{-1}), the decrease of db-OH integrated absorbance is well fitted by an exponential function (de Barros et al. 2015a).

The db-OH integrated absorbance, analyzed in the 3700–3560 cm^{-1} range, decreases exponentially with a compaction cross-section σ_c. For the H_2O:CO mixtures (3:2) and (10:1), $\sigma_c \sim 1.1 \times 10^{-11}$ cm^2 and 1.2×10^{-11} cm^2, respectively (see Fig. 6 of Seperuelo Duarte et al. (2021)).

3.2 Precursor molecules

Three H_2O vibrational bands are observed at 3279, 1657 and 760 cm^{-1}. For CO are observed at 2151, 2138 cm^{-1} and 2088 cm^{-1} for ^{13}CO bands. Spectroscopic data of the precursor bands used for the cross sections calculations are displayed in Table 1.

The knowledge of band strength ($A_{value} \equiv A_v$) is required to obtain the column densities, N(F), from both astronomical and laboratory spectra, and allows one to obtain the molecules abundances in the outer solar system and in the ISM. The Lambert-Beer equation was used to convert integrated absorbances, $S(F)$, into column densities, N(F), for all fluences, F. **Using the (A-values) display in Tables 1 and 2,** the column density N (F) of absorbers can be obtained by the standard equation given by:

$$N(F) = ln10 \frac{\int_{\upsilon_{i,1}}^{\upsilon_{i,2}} \tau_{i,1} d\upsilon_{i,1}}{A_{value}(\upsilon_{i,1})} = ln10 \frac{S(F)}{A_v} \quad (1)$$

where $\tau_{i,\nu}$ is the optical depth of i mode in H_2O:CO ice at frequency $\upsilon_{i,1}$ and $\upsilon_{i,2}$ are the lower and upper integration boundaries in cm^{-1}, respectively, for the absorption of the i feature.

The CO and H_2O column densities were determined by using Eq.(1) for the 2138 cm^{-1} band and for the 760 cm^{-1} band, since the 3279

Table 2. Molecular bands observed in the current work for the H_2O:CO (3:2) and (10:1) ice mixtures. Wavelengths; absorption modes, A-values and references.

Position H_2O:CO (3:2) (cm^{-1})	Position H_2O:CO (10:1) (cm^{-1})	Literature values (cm^{-1})	Identified molecules	Absorption mode	A-values ($\times 10^{-17}$ cm $molecule^{-1}$)	Reference
4684.3	4683.0	4685	CO_2	$2\nu_3$	-	*a*
4282.8	4279.8	4280/4270	CH_3OH	$\nu_2/\nu_9 + \nu_7$	-	*b*
3707.0	3706.7	3707	CO_2	$\nu_1 + \nu_3$	0.14	*a,c,d,r,n*
3599.8	3599.8	3602	CO_2	$2\nu_2 + \nu_3$	0.05	*a,b,d*
3274.2	3288.5	3339	H_2O_2	$\nu_2 + \nu_6$	-	*e*
2853.5	2853.1	2850	H_2O_2	$\nu_2 + \nu_6$	5.7	*e,f*
2342.5	2343.0	2346.0	CO_2	ν_3	7.6	*a,b,c,r,n*
2278.0	2278.5	2278.0	$^{13}CO_2$	ν_3	7.8	*b,c,d,i,r*
2242.0	2243.0	2242	C_3O_2	ν_3	13.0	*n,o*
2193.0	*	2193	C_3O_2	ν_1	-	*d,n*
1875.3	1874.6	1863/1883	HCO	ν_2 (CO stretch)	1.5	*b,g,s*
1853.3	1854.7	1853/1847	HCO/HOCO**	ν_3 (CO stretch)	2.1/1.5	*b,g,l,s*
1694.6	1695.5	1710	HCOOH	ν_S (C=O)	6.7	*b,j*
1495.7	1494.4	1496	H_2CO	ν_3 (CH scissoring)	0.4	*b,r/g,s*
1427.0	1426.4	1428	$H_2CO/CH_3OH/CH_3CHO$	$\nu_4/\nu_6/\nu_8/\nu_5$ (OH + CH rocking)	0.9/0.37	*b,p,s*
1382.0	1381.0	1381	$HCOO^-$**/HCOOH	δ(CH)	0.26	*b,j*
1248.0	1250.0	1247	H_2CO	ν_6	0.15	*g,j,r*
1243.3	*	1244.0	H_2CO	ν_8/ν_9	0.1	*k,r*
1222.1	1223.0	1219	HCOOH	ν_{12}/ν_8	1.5	*b,j,l*
1132.2	1131.0	1130	CH_3OH	ν_7, ν_{11}	0.13	*b,j*
1090.0	1089.0	1088/1078	HCO/C_2H_5OH	ν_2/ν_9 (CH rocking)	0.55/0.66	*b,g,l*
1049.2	1048.5	1047	CH_3OH	ν_8	1.53	*b*
1039.0	1039.5	1039	O_3	ν_6	0.6	*e*
882.0	876.9	886	H_2O_2	-	0.0302	*e*
655.9	660.3	660	CO_2	ν_2	1.1	*a,b,c,d,q*

[a] Bernstein et al. (2005), [b] Bennett & Kaiser (2007a); [c] Gerakines et al. (1994); [d] Jamieson et al. (2006); [e] Loeffler et al. (2006); [f] Moore & Hudson (2000); [g] Gerakines et al. (1996); [h] Elsila et al. (1997); [i] Boduch et al. (2012); [j] Schutte et al. (1999); [k] Schutte et al. (1993); [l] Hudson & Moore (1999); [m] Dibben et al. (2000); [n] Seperuelo Duarte et al. (2010); [o] Gerakines & Moore (2001); [p] Bennett et al. (2005a); [q] Bennett et al. (2005b); [r] Bouilloud et al. (2015); [s] Bennett & Kaiser (2007b).

* Not seen/or very small feature for (10:1) H_2O:CO concentration.** Jiménez-Escobar, et al. (2016)

cm^{-1} band had saturated for the (10:1) concentration, respectively. Since, at the sample surface, the precursor column densities decrease with F and the product´s concentrations increase, the precursor sputtering yields must decrease exponentially. Under these conditions, the evolution of each precursor column density due to sputtering becomes similar to that caused by molecular dissociation, which means that FTIR spectroscopy is only sensitive to the net effect of both processes (Mejía et al. 2013). If the concentration of a given molecular species at the target surface were be constant during the bombardment, its sputtering yield Y would also be constant and its column density would decrease linearly with F: this is not observed. Taking exponential behavior into account, for each precursor species i, N_i(F) writes:

$$N_i(F) \equiv N_{i,0} \exp(-\sigma_{d,i} F) \tag{2}$$

were $\sigma_{d,i} = \sigma_d + Y_0/N_0$ is the apparent destruction cross section, σ_d is the usual destruction cross section, Y_0 is the initial sputtering yield, and N_0 is the initial column density. It is important to mention that if layering (particularly of water molecules) occurs during the irradiation, the precursor's Y_0 is progressively reduced to zero, after a certain time, so that the measured $\sigma_{d,i}$ tends to σ_d. Table 2 shows the formation and destruction cross sections values obtained for the H_2O and CO precursors determined by using Eq.(2). More details on the precursor structural changes and the cross sections can be found at Seperuelo Duarte et al. (2021).

3.3 Chemical process: formation of products

Figures 2 and 3 show the Mid-IR spectra of the non-irradiated and irradiated H_2O:CO (3:2) and (10:1) ice mixtures at fluences from $0 - 1.0 \times 10^{13}$ and $0 - 1.5 \times 10^{13}$ ions cm^{-2}, respectively. Table 2 lists the main bands observed in IR spectra constituted by the vibrations of precursor and product molecules for both H_2O:CO ice concentrations.

The primary radiation effects are the ionization and molecular excitation along the projectile tracks. Ionization of molecules causes radicals be formed which can induce chemical reactions. A diagram is proposed to show the possible formed molecules during radiolysis in Fig.4. For the case of water, H_2O, both H and OH radicals can undergo radical-radical reactions either to reform H_2O, generate H_2 and H_2O_2, or even to dissociate to form the species H_2 and O_2. The H_2 and O_2 are homonuclear molecules and do not exhibit any band in the IR spectrum. However, O_3 formation is observed at 1039 cm^{-1} for the (3:2) and (1:10) concentrations. Ozone was also observed in the O_2 and H_2O radiolysis

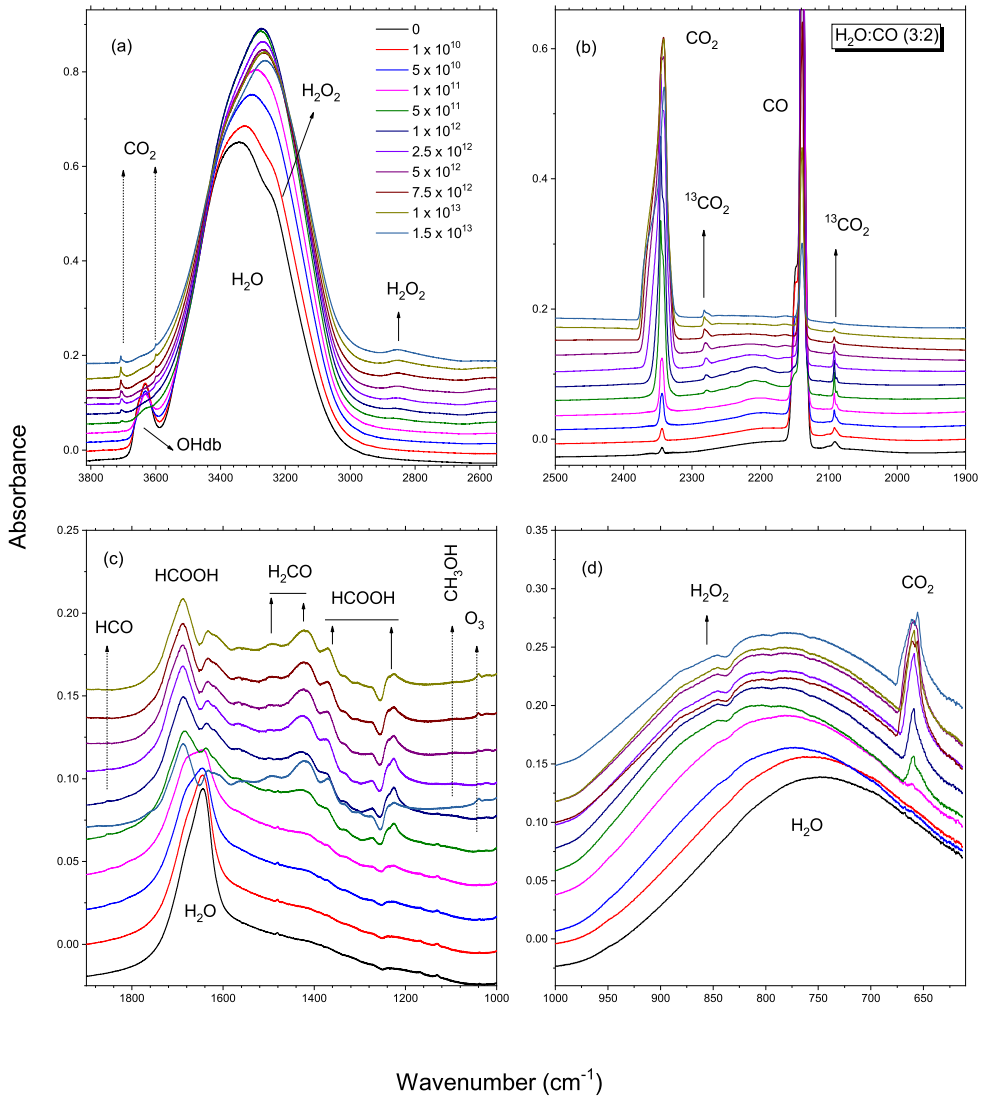

Figure 2. Mid-IR spectra of the non-irradiated and irradiated H_2O:CO (3:2) ice at fluences within 0 - 1.5 × 10^{13} ions cm^{-2}. Spectral regions: (a) 3380 to 2600 cm^{-1}, (b) 2400 to 2000 cm^{-1}, (c) 1900 to 1150 cm^{-1} and (d) 1960 to 630 cm^{-1}.

experiments carried out by Elsila et al. (1997); Loeffler et al. (2006) and Boduch et al. (2012). The two simplest pathways for O_3 formation are (i) by O-atom addition and (ii) by O-atom transfer from a hydroxyl radical(OH).

Similarly to the pure CO ice radiolysis, CO_2 is the most abundant observable molecular species formed in the ice. Carbon monoxide, CO and the hydrogen from H_2O can undergo to radical-radical reactions forming CO_2 and hydrocarbon molecules. This may happen also via reactions transforming three CO molecules into CO_2 + C_2O, or from four CO molecules into C_3O_2 + CO_2. Moreover, C_nO_m molecules, with two or more carbon atoms, have also been produced in CO radiolysis experiments (Jamieson et al. 2006; Seperuelo Duarte et al. 2010). Product bands due to the precursor carbon dioxide ($^{12}CO_2$ and its isotope $^{13}CO_2$) were observed at 4684, 3707, 3599, 2343, 655, 2278 and 2092 cm^{-1}, respectively (Hudson & Moore 1999; Trottier & Brooks 2004; Loeffler & Baragiola 2005; Bernstein et al. 2005; Bennett et al. 2005b; Jamieson et al. 2006; Bennett & Kaiser 2007a; Seperuelo Duarte et al. 2010). Observed IR features at 2193 cm^{-1} and 2242 cm^{-1} may be attributed to the carbon suboxide, or tricarbon dioxide (C_3O_2) band, and carbon dioxide (CO_2).

Alternatively, two CO molecules may react with water molecules, forming acetaldehyde (CH_3COH), which is observed through very small

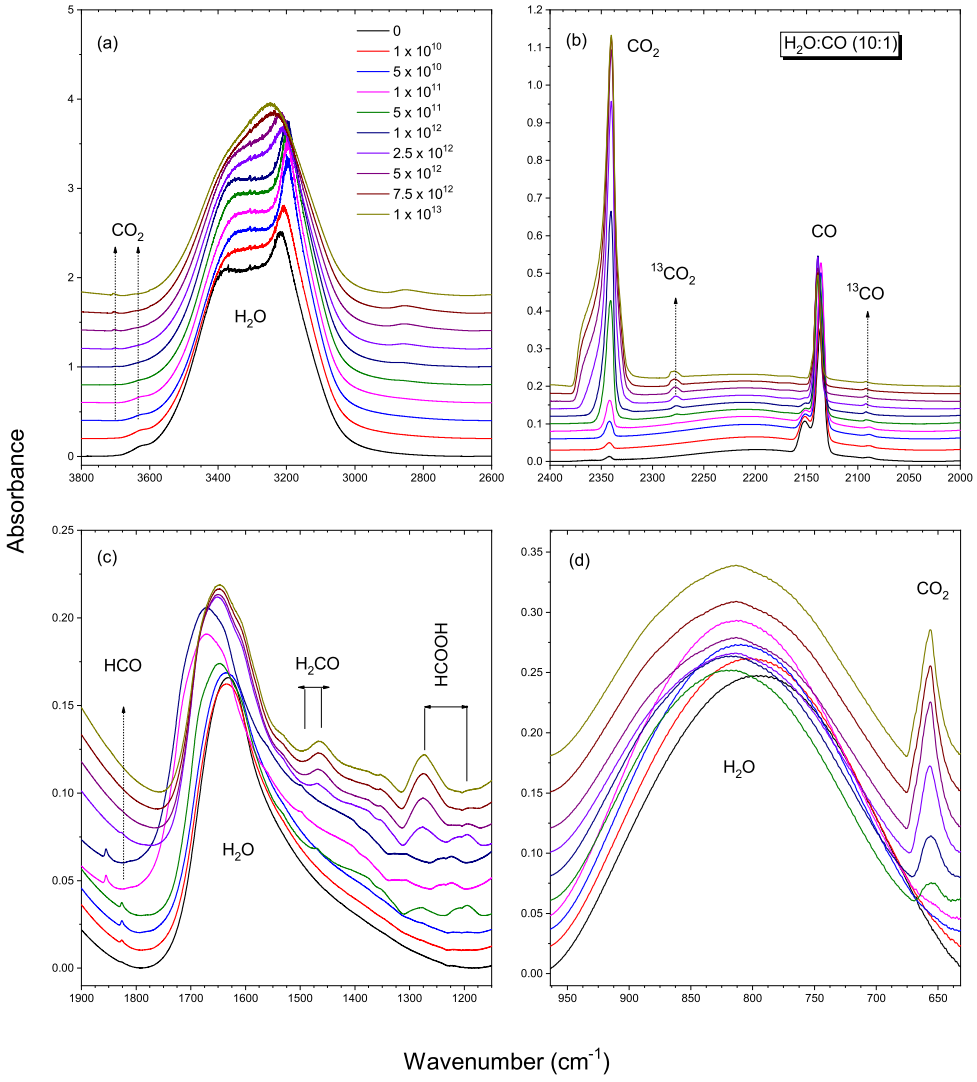

Figure 3. Mid-IR spectra of the non-irradiated and irradiated H_2O:CO (10:1) ice at fluences within 0 - 1.0 × 10^{13} ions cm^{-2}. Spectral regions: (a) 3380 to 2600 cm^{-1}, (b) 2400 to 2000 cm^{-1}, (c) 1900 to 1150 cm^{-1} and (d) 1960 to 630 cm^{-1}.

bands at ∼ 1332, 1371, 1426 cm^{-1} (Bennett et al. 2005a,b) and through the ozone (O_3) band at 1039 cm^{-1} (Gerakines et al. 1996; Hudson & Moore 1999; Bennett et al. 2005a; Bennett & Kaiser 2007a).

Formic acid (HCOOH) is efficiently formed in H_2O:CO radiolysis. It is identified by the vibrations at 1694 cm^{-1} (Bennett & Kaiser 2007a), 1381 cm^{-1} (Schutte et al. 1999; Bennett & Kaiser 2007a) and 1220 cm^{-1} (Schutte et al. 1999; Hudson & Moore 1999; Bennett & Kaiser 2007a). Hudson & Moore (1999) suggested HCCOH molecule is formed via HCO + OH or H_2 + CO_2. The formyl radical (HCO) is identified by the vibrations at 1885, 1854 cm^{-1} (Gerakines et al. 1996; Hudson & Moore 1999; Bennett & Kaiser 2007a) and 1090 cm^{-1} (Gerakines et al. 1996; Hudson & Moore 2000; Bennett & Kaiser 2007a). Following the results of Hudson & Moore (2000), HCO is considered an intermediate product in the formaldehyde (H_2CO) formation.

The formaldehyde is identified by its vibrations at 1495 cm^{-1} (Hudson & Moore 1999; Gerakines et al. 1996; Bennett & Kaiser 2007a), 1332 cm^{-1} (Bennett & Kaiser 2007a), 1248 and 1244 cm^{-1} (Schutte et al. 1993; Gerakines et al. 1996). In the current work, H_2CO is easily identified and may be seen as an intermediate compound for the formation of methanol (CH_3OH), following the possible sequence H_2 + H_2CO. The CH_3OH molecules are identified by their vibrations at 4279, 1426, 1131 and 1049 cm^{-1} (Bennett & Kaiser 2007a; de Barros et al. 2011).

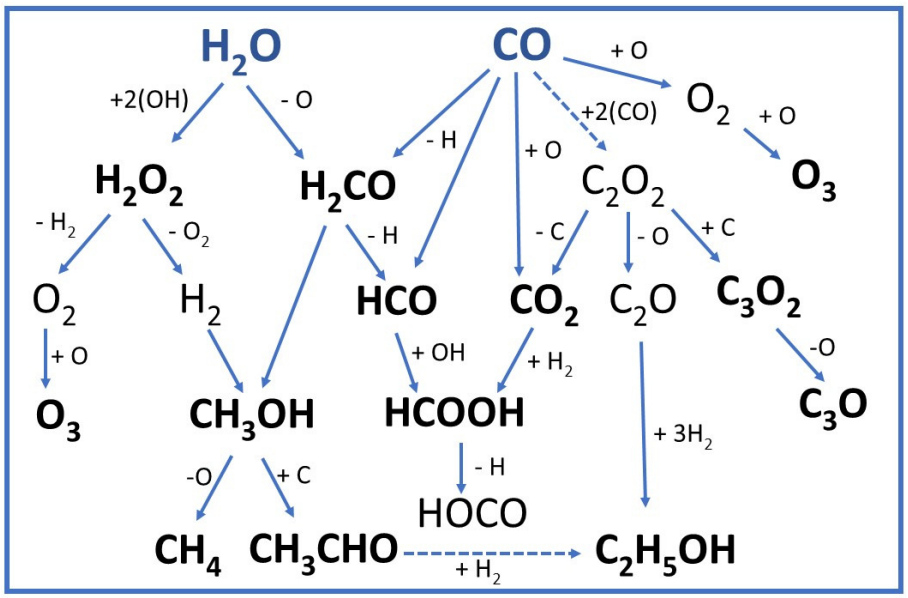

Figure 4. Proposed diagram for the water and carbon monoxide dissociation and for the successive chemical reactions. The molecules in bold correspond to the ones observed in Figs. 2 and 3, their **measured** cross-sections are shown in Table 3.

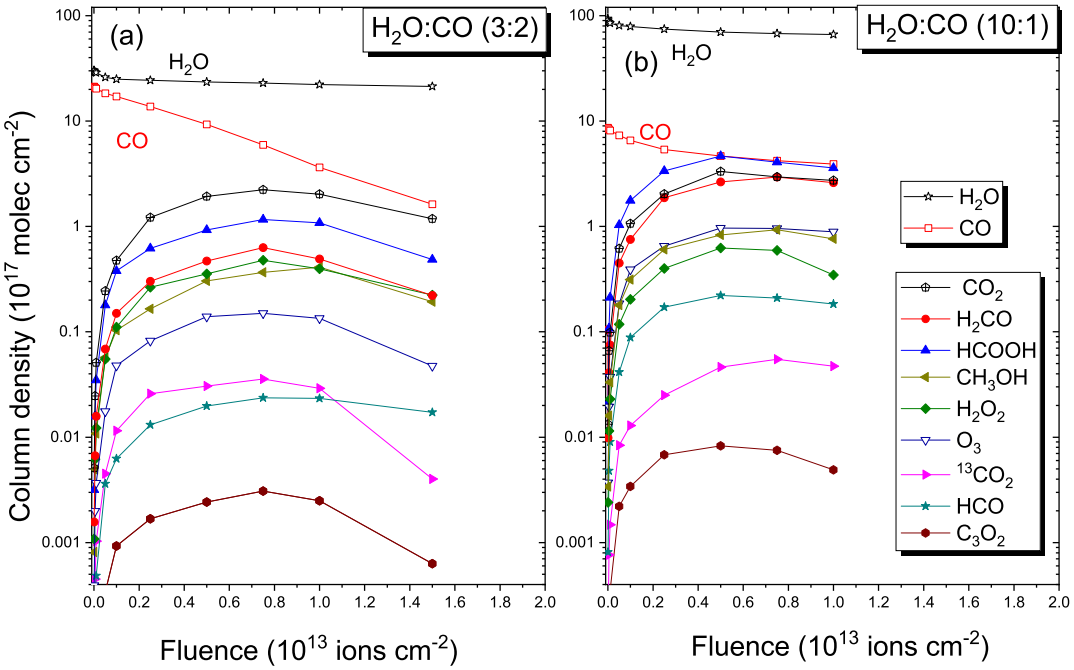

Figure 5. Dependence on fluence of the products's column densities, for H_2O:CO (3:2) and (10:1) concentrations. Solid lines are aids to guide the eyes.

We were unable to identify any absorption band of the acetyl radical [CH_3CO], expected at 1840 cm^{-1}, 1330 cm^{-1} and 1420 cm^{-1} region (Jacox, M. E. 1982). We also could not identify any methane band. The possible CH_4 at 3010 cm^{-1} band (Gerakines et al. 1996) is hidden in the foot of the OH-strech mode (3200 cm^{-1}) of water molecule.

Figures 5 (a) and (b) show the column density evolution of products formed in the H_2O:CO radiolysis for the (3:2) and (10:1) concentrations, respectively. Column densities are determined from the measured integrated absorbances and from the A-values presented in Table 2.

Table 3. Wavelengths, formation (σ_f) and destruction ($\sigma_{d,j}$) cross sections of products. Cross sections were obtained by fitting the product´s column density evolutions with Eq. (3). **Errors vary between 5 to 30 %, obtained by fitting N(F) evolution with Eq. (3).**

Molecules	Frequency cm^{-1}	σ_f 10^{-15} cm^2	σ_d 10^{-13} cm^2	σ_f 10^{-15} cm^2	σ_d 10^{-13} cm^2
		H_2O:CO	(3:2)	H_2O:CO	(10:1)
CO	2138.2	-	(1.6 ± 0.4)	-	(0.35 ± 0.03)
H_2O	760.0	-	(0.15 ± 0.08)	-	(0.25 ± 0.07)
CO_2	2342.5	(20.5 ± 1.5)	(2.4 ± 0.5)	(35.4 ± 2.3)	(2.2 ± 0.3)
H_2O_2	2853.5	(3.1 ± 0.7)	(2.3 ± 0.3)	(2.5 ± 0.8)	(1.5 ± 0.2)
HCOOH	1380.5	(5.8 ± 0.6)	(3.2 ± 0.7)	(9.4 ± 1.4)	(4.3 ± 0.6)
H_2CO	1495.7	(4.1 ± 0.6)	(3.3 ± 0.7)	(8.7 ± 1.0)	(3.5 ± 0.5)
CH_3OH	1132.2	(1.9 ± 0.4)	(2.6 ± 0.7)	(6.4 ± 0.5)	(1.7 ± 0.3)
$^{13}CO_2$	2278.0	(0.48 ± 0.08)	(6.4 ± 0.7)	(1.5 ± 0.3)	(2.5 ± 0.4)
HCO	1875.3	(0.13 ± 0.05)	(5.5 ± 0.6)	(0.28 ± 0.05)	(7.7 ± 0.9)
C_3O_2	2242.0	(0.050 ± 0.008)	(8.7 ± 1.2)	(0.38 ± 0.07)	(6.1 ± 0.6)
O_3	1039.0	(0.7 ± 0.1)	(4.7 ± 0.6)	(2.9 ± 0.5)	(3.7 ± 0.5)

3.4 CO and H_2O formation and destruction cross sections and their products

As described in Section 3.2, since chemical reactions in the target are involved, the methodology for determining the formation cross section of products becomes less obvious. The following procedure is used to get the formation and destruction cross sections of precursors constituted by the H_2O:CO ice mixture. If the production of the formed species j occurs directly from a given precursor i without interference of the evolving environment, its normalized column density writes:

$$\frac{N_j(F)}{N_{i,0}} = \frac{\sigma_{f,j}}{\sigma_{d,i} - \sigma_{d,j}}[\exp(-\sigma_{d,j}F) - \exp(\sigma_{d,i}F)] \quad (3)$$

For hybrid molecules, $i > 1$ precursor species are involved; Eq. (3) is still valid, however the precursor column density $N_{i,0}$ is now interpreted as corresponding to the precursor group (de Barros et al. 2015a, 2016, 2017). If at least n molecules of the same species i are necessary for forming the observed new species, Eq. (3) also is employed but $N_{1,0}/n$ is considered as the precursor column density. Keeping for example, $N_{1,0}$ fixed for H_2O or CO. This is equivalent to considering synthesis involving n precursor molecules as a process less efficient than dissociation of a single molecule; its cross section is then "reduced" by a factor n. In this sense, $n = 2$ was considered for the production of the CO_2 and HCOOH (from H_2O + CO) and CH_3CHO (from $2H_2O$ + 2CO + O_3) (Goldanskii et al. 1973). Table 3 presents the formation (σ_f) and destruction (σ_d) cross sections of the observed formed species. Figs. 5 (a) and (b) show, for each product, how its column density evolves with fluence, for the of H_2O:CO (3:2) and (10:1) mixtures respectively. The fittings of the products column densities N(products) by N(precursors), at non irradiated fluence (F = 0), for the H_2O:CO (3:2) and (10:1) radiolysis are shown in Figs. 6a and 6b respectively. **The error bars in Fig. 6 are relatively small, less than 10%; the analyzed bands are well defined, with large signal/noise ratio. Eq. (3) seems to be adequate, so that the quality of the fitting is quite good, as can be appreciated by the agreement shown in Fig. 6. The relative errors on cross sections (Table 3) vary between 5 to 30%. These error ranges are typical for this kind of experiment (de Barros et al. 2011, 2014).**

4 DISCUSSION

4.1 Evolution of Porous Amorphous Ices Mixtures

When comparing the IR spectra intensities of the two ices, it is found that the db-OH in the (3:2) ice db-OH absorbance is five times greater than that of the (10:1) ice. This disproportion indicates a larger number of pores in the ice (3:2) than in the (10:1). To explain this fact, Lauck et al. (2015) suggested that CO molecule interacts with a H_2O molecule in the porous surface, resulting in an increase of the db-OH band absorbance and of the "polar" band of CO located at 2137 cm^{-1}.

The pores collapse is related to the collapse of the water bonds during the few irradiation doses, D < 2 eV $molec^{-1}$. The linear relationship $\sigma_c = S_e/D_0$ gives D_0 values of 0.14 (3:2) and 0.12 (10:1) eV $molec^{-1}$, values lesser than 0.2 eV $molec^{-1}$ found by (Mejía et al. 2015b). This discrepancy may be attributed to the high diffusion of CO molecules or products into surface porous around the ion tracks, reducing the db-OH vibrations.

4.2 Carbon, Oxygen and Hydrogen Budget

The "atom budget" is the balance between the measured number of atoms of each atomic species remaining in the sample as function of fluence. Each elemental budget is addressed by verifying whether the atomic column density of the destroyed compound can account for the atomic

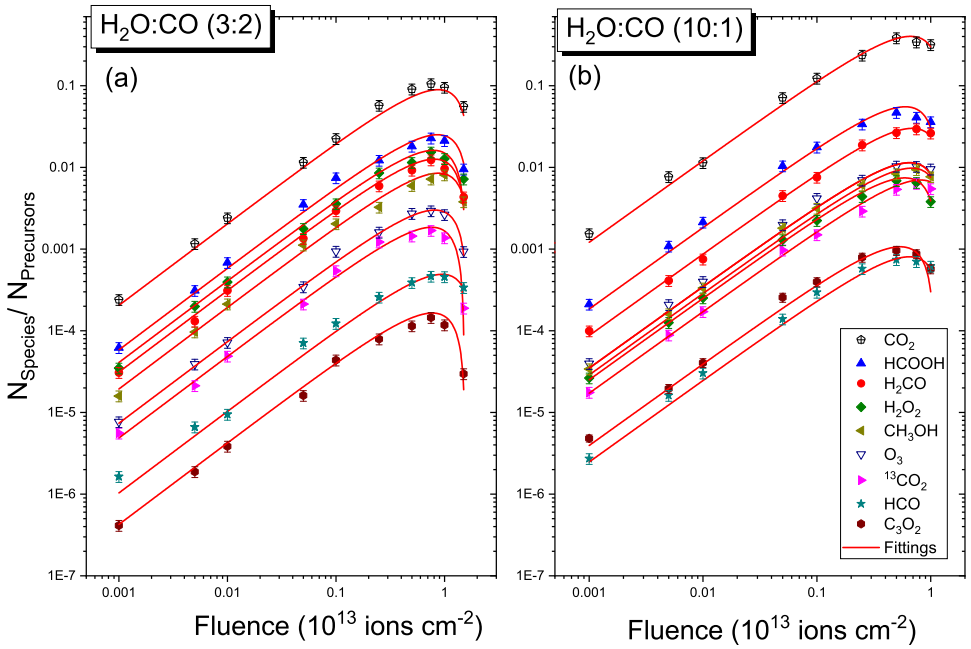

Figure 6. Column densities evolution of product species produced by the H_2O:CO (3:2) and (10:1) radiolysis. Solid curves are fittings performed with Eq. (3). Data are normalized to N_0 and exhibited in log-log scale to stress the linear dependence on F at low fluences.

column densities of the formed products. The column density variations of the H, C and O atoms are determined from the measured molecular column densities, from the precursor concentrations and from the stoichiometry of products. They are compared with initial quantities.

The column density evolution of products formed in the (3:2) and (1:10) ice mixtures are presented in Fig. 7 (a) and (b), respectively. In this experiment, the final number of hydrogen and carbon observed are double for the (10:1) concentration compared to (3:2), and 1.5 times higher for the (10:1) concentration compared to (3:2) one. We expect to determine more hydrogen and oxygen atoms in the (10:1) mixture, but we must take into account that the H atoms, due to H_2O dissociation, diffuse and escape partially from the ice - mainly as H or H_2 - as well as the O atoms from H_2O and CO dissociation - mainly as O or O_2 their budgets are not taken into account because they are IR inactive. For the H, C and O atom budgets, their sputtering is not directly measured. In addition, the deposited molecules (as H_2O of the residual gas, that are less than 10^{15} cm^{-2} - details in Mejía et al. (2020)) on the rear side of the substrate are detected by FTIR but do not interact with the ion beam.

4.3 Atomic sputtering yield

The atomic sputtering yield can be calculated by determining, for each chemical element ejected, its column density evolution with ion beam fluence (Mejía et al. 2020). Indeed, at any time or fluence, the atomic column density decrease **rate of each atomic species must** be equal to its emission rate. The number of sputtered atoms of species k per surface area and during the fluence dF irradiation is $Y_k^a(F)dF$, where Y_k^a is the corresponding atomic sputtering yield, assumed constant during the irradiation.

The conservation law for the number of atoms of any chemical element k can be written as:

$$N_k^a(F) = N_{0,k}^a - Y_k^a(F) \tag{4}$$

where $N_{0,k}^a$ is the initial (atomic) column density of the chemical element k (carbon, oxygen or hydrogen for the current analysis), and Y_k^a the atomic sputtering yield of the same chemical element.

Observing the results obtained by Eq. (4) and shown in the left of Fig. 8 for the (3:2) concentration, **the decreasing rate is** 4, 7, and 14 ($\times 10^4$) atoms ion^{-1} for the H, C, and O column densities, respectively. Comparing these three Y_k, **Y, surprisingly, the H atoms** appear not be sputtered as quickly as the C and O atoms, owing to H atoms reacting with radicals or with excited species (e.g., C, O, CO^*, HO^*) to synthesize the observed new species listed in Table 2. The rate for C, is almost two times lesser than for O atoms. However, caution must be applied, as this high rate of O might be caused by the unseen O_2 molecules.

As far as total sputtering, Y_T, is concerned, it is useful to quantify it by atomic mass units (u) instead of by the number of atoms. Thus, the total sputtered is approximately $Y_T = Y_H + 12\ Y_C + 16\ Y_O = 2.5 \times 10^6$ u ion^{-1}. At F = 1×10^{13} ion cm^{-2}, the total sputtered per area unit

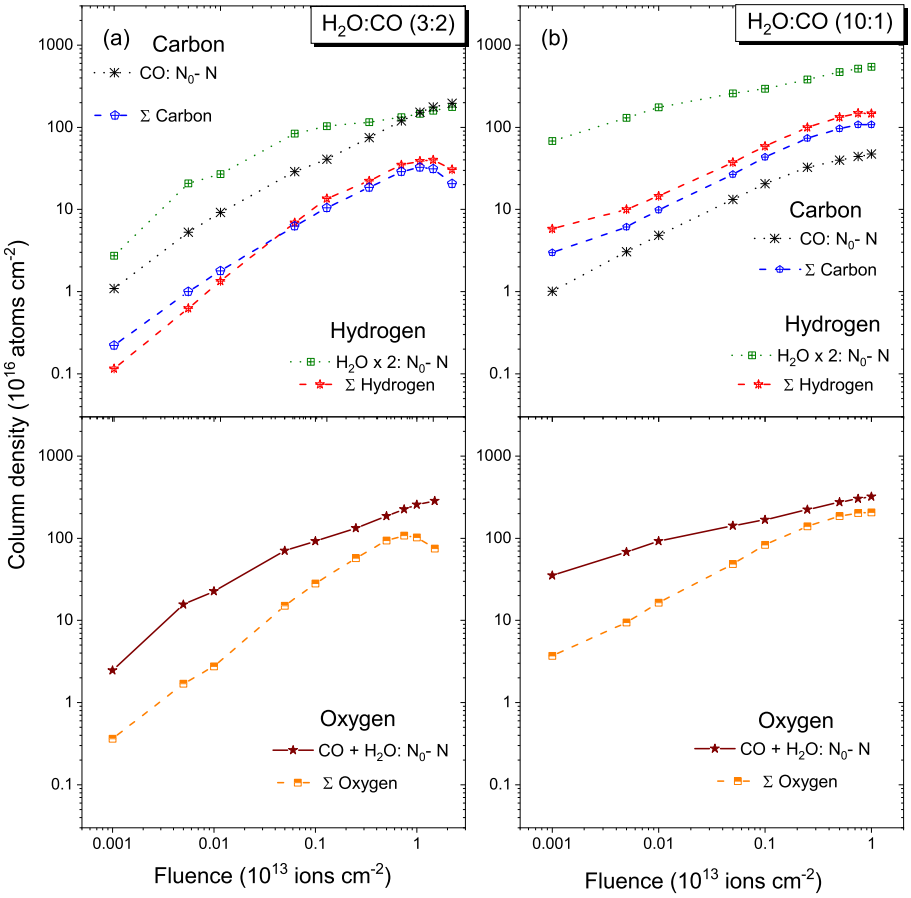

Figure 7. The H (green cross-squares), C (asterisks) and O (brown stars) atomic column density, delivered from dissociation's in the H_2O:CO (3:2) (a) and (10:1) (b) mixtures ice, as a function of fluence. These values are compared with the sum of the same elements (red stars, blue cross-pentagons and orange cross-triangles, respectively) in the molecular products.

from the ice is about 2.5×10^{19} **u cm**$^{-2}$. From Table 1, the initial ice film mass was 10.7×10^{19} **u cm**$^{-2}$, thereby near 25% of the initial mass ice was lost as a result of dose irradiation of 15.8 eV molec^{-1}.

Regarding the (10:1) ice, the *H*, *C* and *O* initial concentrations must be 20:1.0:11, while the observed relative atomic sputtering yields are 6.5:1.0:10. These results indicate that the measured hydrogen sputtering is lower than expected. Since the H_2O dissociation (source of the delivered H atoms) is well monitored, H-product concentrations are underestimated, probably due to H_2 and free H atoms existing in the sample or being desorbed. **Assuming no water leaking into the chamber during the irradiation and** considering the measured atomic sputtering yields, the total atomic yield is about 2×10^6 **u ion**$^{-1}$. At the final fluence, the total sputtered mass from the surface ice was 2×10^{19} **u cm**$^{-2}$, which corresponds to 10% of film mass lost after 15 eV molec^{-1} of deposited dose.

Together, these results provide new insights into the sputtering yields of mixed ices. These findings suggest that Y_T can be calculated by including stoichiometry of all molecules observed in the ice bulk. In the literature, the sputtering yields for pure CO and H_2O ices as a stopping power function were studied by Seperuelo Duarte et al. (2010) and Dartois et al. (2015), respectively. To illustrate this, we consider that 46 MeV $^{58}Ni^{11+}$ transfers 15 eV molec^{-1} dose to pure ices, the total sputtered mass is 1.8×10^{19} **u cm**$^{-2}$ for CO ice, while for H_2O it is 5.4×10^{17} **u cm**$^{-2}$. The comparison in the total sputtered mass between the (3:2), (10:1), (1:0), and (0:1) ices indicate that the presence of CO molecule in H_2O matrix enhances the total sputtered mass considerably. This discrepancy could be attributed to different crystalline or amorphous phases of mixed ices. These findings could also be a consequence of alterations of intermolecular forces of those mixed ices that increases the sputtering process (Mejía et al. 2020).

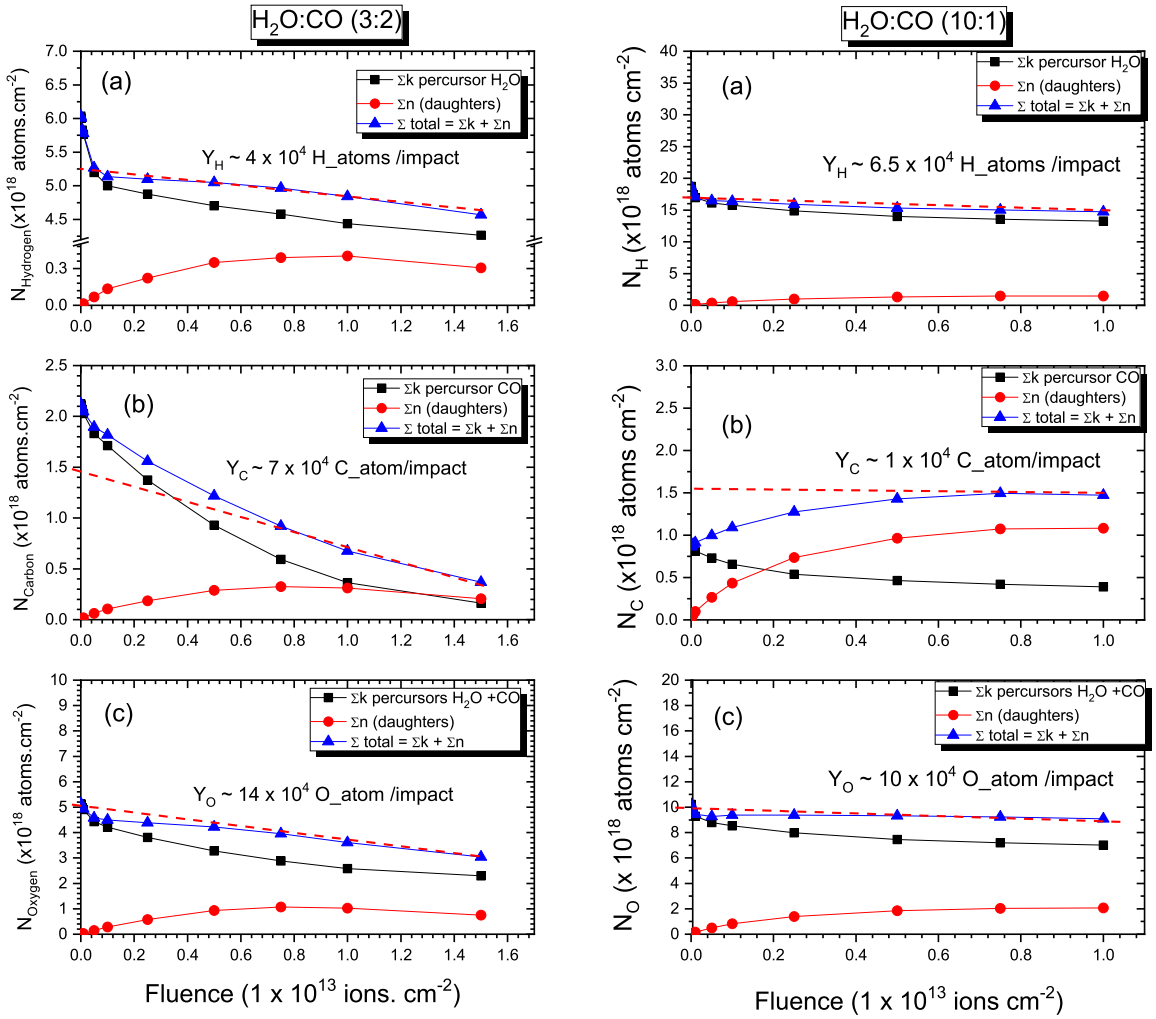

Figure 8. Total atomic column density evolution as a function of fluence, for oxygen, carbon and hydrogen atoms. Data on left correspond to the (3:2) concentration and on the right the (10:1) concentration. Triangles for precursors, squares for the most abundant products and circles for all (sum). (a) for hydrogen and carbon, and (b) for oxygen. The total atomic sputtering yield is Y_0 for each ice mixture.

5 ASTROPHYSICAL IMPLICATIONS

5.1 Comparative results in the ISM environments

The H_2O and CO molecules in the solid phase have been observed in interstellar environments of quiescent regions, in the central and external galaxies, and in low, intermediate, and high massive young stellar objects (LYSOs, IYSOs, and MYSOs). The molecular composition of **grain's icy mantles** also includes many $H_xC_yO_z$ species in a lower percentage with respect to water. Table 4 illustrates the chemical composition of $H_xC_yO_z$ containing ices (adapted from Boogert et al. (2015)); the molecular composition of comets are also showed (adapted from Mumma & Charnley (2011)). The displayed results reveal that molecular astronomical percentages are comparable to those obtained after 15 eV molec^{-1} of deposited dose in current experiments, as presented in the two last columns of Table 4.

In both experiments, a large amount of the molecule precursor CO is consumed to synthesize the new products. What is striking about the product´s concentrations is that they are in the range of those found in ices of the ISM, circumstellar envelopes, and even comets. Table 4 shows the relative concentration of the most abundant molecules in descending order. The H_2O_2 is the most abundant species in the (10:1) ice, unlike the (3:2) ice, where its concentration is about 30 times lesser than in the (10:1) ice. The H_2O_2 molecule has only been detected in comets, and its observation in other astrophysical environments is likely because one of its IR absorption is near the water OH-stretch band. The molecular

Table 4. Relative concentration of molecules in solid phase observed in MYSO, LYSO, BG Stars, and Comets. Relative concentrations of the (3:2) and (10:1) ices after the irradiation dose of 15 eV molec^{-1}. H_2O concentration is normalized to 100 for all situations.

Molecules	MYSO[a]	LYSO[a]	BG Stars[a]	Comets[b]	3:2[c]	10:1[c]
H_2O	100	100	100	100	100	100
CO	3-26	3-85	9-67	0.4-30	20	16.7
H_2O_2	–	–	–	2-17	0.6	18.3
H_2CO	2-7	6	–	0.11-1	4.25	11.2
CO_2	11-27	12-50	14-43	4-30	10	10
HCOOH	0.5-6	0.5-4	<2	0.06-0.14	0.25	6.7
^{13}CO	–	–	–	–	0.15	4.3
CH_3OH	3-31	1-25	1-12	0.2-7	0.01	0.56
HCO	–	–	–	–	0	0.43
O_3	–	–	–	–	0.1	0.35
C_3O_2	–	–	–	–	0	0.01

***Note: The molecular percentages were adapted from: [a] Boogert et al. (2015), [b] Mumma & Charnley (2011), and [c] This work.**

Table 5. Values of the proportionality constant (C), obtained by the power law, evaluated as C = $\sigma_{f,d}/S_e$, where C_f and C_d correspond to the formation and destruction cross sections constant respectively.

Molecules	C_f ($10^{-20}(\mu$/keV$)^{3/2}$)	C_d ($10^{-20}(\mu$/keV$)^{3/2}$)
H_2O	–	10.5
CO	–	14.7
CO_2	3.12	52.3
$^{13}CO_2$	0.801	51.9
C_3O_2	0.089	87.9
O_3	0.325	73.5
H_2O_2	5.49	52.7
HCO	0.430	73.1
H_2CO	4.43	57.0
CH_3OH	0.530	71.3
HCOOH	0.325	56.9

abundances of H_2CO, CO_2, HCOOH and CH_3OH are in the range of these observed molecules. Some molecular species (such as: ^{13}CO, HCO, O_3 and C_3O_2) are so far undetected in astrophysical **ices, probably because - in infrared spectrometry - at least** few monolayers are required to allow detection of a specific absorption band. **Identification of other** complex organic molecules (COMs) have been suggested in Table 2. Their presence in astrophysical ices is questionable, however many of them have been detected in the gas phase (McGuire 2018).

The results of the current work can be used to estimate a time scale for the radiolysis in the ISM ices. The methodology used here is similar to to the one used in the recent work (Seperuelo Duarte et al. 2021). **The column density evolution of each formed species is fitted by Eq. (5). Furthermore, substituting** σ = RΦ, **where R is the processing Rate, and F = Φt in this equation, one gets Eq. (5) which describes** the column density evolution as a function of time (t):

$$\frac{N_j(F)}{N_i(t)} = \frac{R_{f,j}}{R_{d,i} - R_{d,j}}[\exp(-R_{d,j}t) - \exp(R_{d,i}t)] \quad (5)$$

where $R_{d,j}$ and $R_{d,i}$ are the cosmic ray destruction rates for the formed species j and for the parent molecules i **is obtained from (Seperuelo Duarte et al. 2021)**, respectively. **Similarly,** $R_{f,j}$ **holds for the formation rate of species** j**. Simple scale laws** ($\sigma_{f,j} = CS_e$ and $\sigma_{d,j} = CS_e^{3/2}$) were adopted and the **coefficient** C_f **and** C_d **are determined from the** σ_f **formation and** σ_d **destruction cross sections, respectively,** obtained in the current work. **Table 5 shows the the proportionality constant coefficient** $C_{f,d}$ **values for each molecular species formed.**

The cross sections were scaled for six different projectiles (H, O, Mg, Si, Fe and Ni) over the $10^{-1} - 10^4$ MeV u^{-1} range using SRIM (Ziegler et al. 2010) are scaled. Shen et al. (2004) have computed the cosmic ray fluxes for H, O and Fe; the fluxes for other species are computed using the relative abundances between them. The cosmic ray processing rates are determined by multiplying the cross sections by the correspondent **flux** Φ. Table 6 shows the cosmic ray processing rates **(the** R_f **and** R_d**)** integrated over the $10^{-1} - 10^4$ MeV u^{-1} range for the six cosmic ray species. Fig. 9 shows the column densities of formed molecules, normalized to the precursor column density, as a function of time.

Table 6. Formation (R_f) and destruction (R_d) rates of galactic cosmic rays, integrated over the 0.1 – 10,000 MeV u^{-1} energy per nucleon range.

Molecules	R_f (10^{-18} s^{-1})	R_d (10^{-18} s^{-1})
H_2O	–	1.72
CO	–	2.41
CO_2	0.512	8.58
$^{13}CO_2$	0.128	8.51
C_3O_2	0.0145	14.4
O_3	0.0533	12.1
CH_4	0.505	7.2
H_2O_2	0.9	8.64
HCO	0.0705	12
H_2CO	0.727	9.35
CH_3OH	0.0869	11.7
HCOOH	0.0533	9.33
CH_3COH	0.0869	11.7

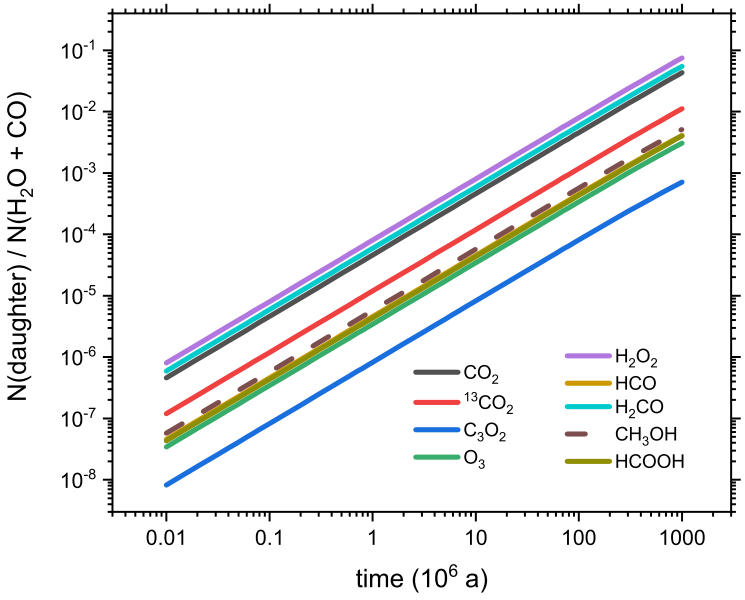

Figure 9. Column density of the formed species, normalized by the parent´s column density, as a function of time.

6 REMARKS AND CONCLUSIONS

We have performed an experimental study of 46 MeV $^{58}Ni^{11+}$ **projectile** interaction with H_2O:CO ice mixture, at (3:2) and (10:1) concentrations, to simulate the physical chemistry induced by heavy and highly charged cosmic rays inside dense and cold ISM regions. This study contributes to the understanding of radiolysis and synthesis of ice mixtures existing in circumstellar envelopes and in the interstellar medium. Results obtained in the current work are:

- For the (3:2) H_2O:CO ice mixture, the destruction cross sections of the CO and H_2O precursors are 1.7×10^{13} and 0.35×10^{13} cm^2, respectively.
- For the (10:1) H_2O:CO ice mixture, these quantities diminish to 0.35×10^{13} and 0.25×10^{13} cm^2, respectively.
- Radiolysis of the H_2O:CO ice mixture produces the following products: CO_2, H_2O_2, O_3, C_3O_2, HCOOH, H_2CO, $^{13}CO_2$, CH_3OH and HCO. The formation and destruction cross sections are determined for both concentrations.
- The abundant products are CO_2, H_2CO, HCOOH, CH_3COH and H_2O_2; the low produced ones are HCO and C_3O_2.
- The observed final *H*, *C* and *O* atom budget ratio for (10:1)/(3:2) are ~ 2.0, 2.0 and 1.5 respectively.
- The total initial atomic sputtering yields, Y_0, for the (3:2) H_2O:CO ice mixture are: 4.0×10^4, 6.2×10^4, and 11×10^4 for *H*, *C* and *O*, respectively.

• The total atomic sputtering yields, Y_T, for the (10:1) H_2O:CO ice mixture are: 6.5×10^4, 1.0×10^4, and 10×10^4 for H, C and O, respectively. The atomic sputtering yield **of oxygen for both mixtures** remains approximately the same.

• An estimate a time scale for the radiolysis in the ISM ice is performed. The results reveal that astronomical molecular concentrations are comparable to those obtained after 15 eV molec^{-1} of deposited dose for the current experiments.

ACKNOWLEDGMENTS

The French-Brazilian exchange program CAPES-COFECUB, as well as the CNPq (INEspaço), CNPq (301868/2017-4 and 407938/2018-4), FINEP (0647/18), FAPERJ (E-26/210.965/2021, E-26/210.801/2021, E-26/245.307/2019 and E-26/241.202/2018) are acknowledged for partial support. This study was financed in part by the Coordenação de Aperfeiçoamento de Pessoal de Nível Superior - Brazil (CAPES) - Finance Code 001. We are grateful to the staff of GANIL and CIMAP, and in particular to T. Been, C. Grygiel and J. M. Ramillon for their invaluable assistance during the experiments.

7 DATA AVAILABILITY

The data underlying this article will be shared on reasonable request to the corresponding author.

REFERENCES

Aikawa, Y., Kamuro, D., Sakon, I., Itoh, Y., Terada, H., Noble, J. A., ... & Kawamura, A., 2012, A&A, 538, A57.
Allamandola, L. J., Sandford, S. A., & Valero, G. J., 1988, Icar, 76(2), 225-252.
Bennett, C. J., Jamieson, C. S., Osamura, Y., & Kaiser, R. I., 2005a, ApJ, 624(2), 1097.
Bennett, C. J., Osamura, Y., Lebar, M. D., & Kaiser, R. I., 2005b, ApJ, 634(1), 698.
Bennett, Chris J., & Ralf I. Kaiser, 2007a, Apj, 661.2, 899.
Bennett, C. J., & Kaiser, R. I., 2007b, ApJ, 660(2), 1289.
Bennett, C. J., Hama, T., Kim, Y. S., Kawasaki, M. A. S. A. H. I. R. O., & Kaiser, R. I., 2010, ApJ, 727(1), 27.
Bennett, C. J., Brotton, S. J., Jones, B. M., Misra, A. K., Sharma, S. K., & Kaiser, R. I., 2013, Analytical chemistry, 85(12), 5659-5665.
Bernstein, M. P., Cruikshank, D. P., & Sandford, S. A., 2005, Icar, 179(2), 527-534.
Boogert, A. C. A., Chiar, J. E., Knez, C., Öberg, K. I., Mundy, L. G., Pendleton, Y. J., ... & Van Dishoeck, E. F., 2013, ApJ, 777(1), 73.
Boogert, A. A., Gerakines, P. A., & Whittet, D. C., 2015, ARAA, 53.
Bouilloud, M., Fray, N., Bénilan, Y., Cottin, H., Gazeau, M. C., & Jolly, A., 2015, MNRAS, 451(2), 2145-2160.
Boduch, P., Domaracka, A., Fulvio, D., Langlinay, T., Lv, X. Y., Palumbo, M. E., ... & Strazzulla, G., 2012, A&A, 544, A30.
Chiar, J. E., Adamson, A. J., Kerr, T. H., & Whittet, D. C. B., 1995, ApJ, 455, 234.
Chiar, J. E., Adamson, A. J., Pendleton, Y. J., Whittet, D. C. B., Caldwell, D. A., & Gibb, E. L., 2002, ApJ, 570(1), 198.
Chiar, J. E., Pendleton, Y. J., Allamandola, L. J., Boogert, A. C. A., Ennico, K., Greene, T. P., ... & Roellig, T. L., 2011, ApJ, 731(1), 9.
Dartois, E., Augé, B., Rothard, H., Boduch, P., Brunetto, R., Chabot, M., ... & da Silveira, E. F., 2015, NIMB, 365, 472-476.
de Barros, A. L. F., Domaracka, A., Andrade, D. P. P., Boduch, P., Rothard, H., & Da Silveira, E. F., 2011, MNRAS, 418(2), 1363-1374.
de Barros, A. L. F., da Silveira, E. F., Pilling, S., Domaracka, A., Rothard, H., & Boduch, P., 2014, MNRAS, 438(3), 2026-2035.
de Barros, A. L. F., da Silveira, E. F., Bergantini, A., Rothard, H., & Boduch, P., 2015a, ApJ, 810(2), 156.
de Barros, A. L. F., Mejía, C., Morgado, W. A. M., Almeida, L. F., & da Silveira, E. F., 2015b. Brazilian Journal of Physics, 45(2), 195-199.
de Barros, A. L. F., da Silveira, E. F., Fulvio, D., Rothard, H., & Boduch, P., 2016, ApJ, 824(2), 81.
de Barros, A. L. F., da Silveira, E. F., Fulvio, D., Boduch, P., & Rothard, H., 2016, MNRAS, 465(3), 3281-3290.
Dibben, M., Szczepanski, J., Wehlburg, C., & Vala, M., 2000. JPCA, 104(16), 3584-3592.
Duley, W. W., 1974, Astrophysics and Space Science, 26(1), 199-205.
Elsila, J., Allamandola, L. J., & Sandford, S. A., 1997, ApJ, 479(2), 818.
Geballe, T.R., 1986, A&A, 210, 345.
Gerakines, P. A., Schutte, W. A., Greenberg, J. M., & van Dishoeck, E. F., 1994, arXiv preprint astro-ph/9409076.
Gerakines, P. A., Schutte, W. A., & Ehrenfreund, P., 1996, A&A, 312, 289-305.
Gerakines, P. A., & Moore, M. H., 2001, Icar, 154(2), 372-380.
Gibb, E. L., Whittet, D. C. B., Boogert, A. C. A., & Tielens, A. G. G. M., 2004, ApJS, 151(1), 35.
Goldanskii V. I., Frank-Kamenetskii M. D., Barkalov I. M., 1973, Science, 182, 1344.
Hama, T., & Watanabe, N., 2013, Chemical reviews, 113(12), 8783-8839.
Hudson, R. L., & Moore, M. H., 1999, Icar, 140(2), 451-461.
Hudson, R. L., & Moore, M. H., 2000, A&A, 357, 787-792.
Hudson, R. L., & Moore, M. H., 2001, JGRP, 106(E12), 33275-33284.
Ioppolo, S., Palumbo, M. E., Baratta, G. A., & Mennella, V., 2009, A&A, 493(3), 1017-1028.
Jacox, M. E., 1982, Chemical Physics, 69(3), 407-422.
Jamieson, C. S., Mebel, A. M., & Kaiser, R. I., 2006, A The Astrophysical Journal Supplement Series, 163(1), 184.
Jiménez-Escobar, A., Chen, Y. J., Ciaravella, A., Huang, C. H., Micela, G., & Cecchi-Pestellini, C., 2016, ApJ, 820(1), 25.
Kerr, T. H., Adamson, A. J., & Whittet, D. C. B., 1993, MNRAS, 262(4), 1047-1056.
Lacy et al. 1984 Duley, W. W., 1974, Astrophysics and Space Science, 26(1), 199-205.
Lauck, T., Karssemeijer, L., Shulenberger, K., Rajappan, M., Öberg, K. I., & Cuppen, H. M. (2015). CO diffusion into amorphous H_2O ices. The Astrophysical Journal, 801(2), 118.

Larson, R. B., 1985, MNRAS, 214(3), 379-398.
Loeffler, M. J., & Baragiola, R. A., 2005, Geophysical research letters, 32(17).
Loeffler, M. J., Teolis, B. D., & Baragiola, R. A., 2006, The Journal of chemical physics, 124(10), 104702.
McGuire, B. A., 2018, ApJS, 239(2), 17.
Mejía, C., de Barros, A. L. F., Bordalo, V., da Silveira, E. F., Boduch, P., Domaracka, A., & Rothard, H., 2013, MNRAS, 433(3), 2368-2379.
Mejía, C., de Barros, A. L. F., Duarte, E. S., da Silveira, E. F., Dartois, E., Domaracka, A., ... & Boduch, P. (2015). Compaction of porous ices rich in water by swift heavy ions. Icarus, 250, 222-229.
Mejía, C., de Barros, A. L. F., Rothard, H., Boduch, P., & da Silveira, E. F., 2020, ApJ, 894(2), 132.
McFadzean, A. D., Whittet, D. C. B., Longmore, A. J., Bode, M. F., & Adamson, A. J., 1989, MNRAS, 241(4), 873-882.
Moore, M. H., & Hudson, R. L., 2000, Icar, 145(1), 282-288.
Moneti, A., Cernicharo, J., & Pardo, J. R., 2001, The Astrophysical Journal Letters, 549(2), L203.
Moultaka, J., Eckart, A., & Schödel, R., 2009, ApJ, 703(2), 1635.
Mumma, M. J., & Charnley, S. B., 2011, A&A 49, 471-524.
Munoz Caro, G. M., Ciaravella, A., Jiménez-Escobar, A., Cecchi-Pestellini, C., Gonzalez-Diaz, C., & Chen, Y. J., 2019, ACS Earth and Space Chemistry, 3(10), 2138-2157.
Noble, J. A., Fraser, H. J., Aikawa, Y., Pontoppidan, K. M., & Sakon, I., 2013, ApJ, 775(2), 85.
Öberg, K. I., Boogert, A. A., Pontoppidan, K. M., Van den Broek, S., Van Dishoeck, E. F., Bottinelli, S., ... & Evans II, N. J., 2011, ApJ, 740(2), 109.
Oliveira, J. M., van Loon, J. T., Sloan, G. C., Indebetouw, R., Kemper, F., Tielens, A. G. G. M., ... & Meixner, M., 2011, MNRAS Letters, 411(1), L36-L40.
Pauly, T., & Garrod, R. T., 2018, ApJ, 854(1), 13.
Pontoppidan, K. M., Fraser, H. J., Dartois, E., Thi, W. F., Van Dishoeck, E. F., Boogert, A. C. A., ... & Bisschop, S. E., 2003, A&A, 408(3), 981-1007.
Pontoppidan, K. M., Dullemond, C. P., van Dishoeck, E. F., Blake, G. A., Boogert, A. C., Evans II, N. J., ... & Lahuis, F., 2005, ApJ, 622(1), 463.
Pontoppidan, K. M., Boogert, A. C., Fraser, H. J., van Dishoeck, E. F., Blake, G. A., Lahuis, F., ... & Salyk, C., 2008, ApJ, 678(2), 1005.
Ryazantsev, S. V., Zasimov, P. V., & Feldman, V. I., 2020, Chemical Physics Letters, 137540.
Seperuelo Duarte, E., Boduch, P., Rothard, H., Been, T., Dartois, E., Farenzena, L. S., & da Silveira, E. F., 2009, A&A, 502(2), 599-603.
Seperuelo Duarte, E., Domaracka, A., Boduch, P., Rothard, H., Dartois, E., & da Silveira, E. F., 2010, A&A, 512, A71.
Seperuelo Duarte, E., de Barros, A. L. F., da Silveira, E. F., Domaracka, A., Boduch, P., & Rothard, H. (2021). MNRAS, 508(3), 4297-4309.
Schutte, W. A., Boogert, A. C. A., Tielens, A. G. G. M., Whittet, D. C. B., Gerakines, P. A., Chiar, J. E., ... & De Graauw, T. H., 1999, A&A, 343, 966-976.
Schutte, W. A., Allamandola, L. J., & Sandford, S. A., 1993, Icar, 104(1), 118-137.
Shen, C. J., Greenberg, J. M., Schutte, W. A., & Van Dishoeck, E. F., 2004, A&A, 415(1), 203-215.
Shimonishi, T., Onaka, T., Kato, D., Sakon, I., Ita, Y., Kawamura, A., & Kaneda, H., 2010, A&A, 514, A12.
Shuping, R. Y., Snow, T. P., Chiar, J. E., & Kerr, T., 2000, ApJ, 529(2), 932.
Soifer, B. T., Puetter, R. C, Russell, R. W., Willner, S. P., Harvey, P. M., and Gillett, F. C., 1979, ApJ (Letters), 232, L53.
Spoon, H. W. W., Koornneef, J., Moorwood, A. F. M., Lutz, D., & Tielens, A. G. G. M., 2000, arXiv preprint astro-ph/0003457.
Spoon, H. W. W., et al, 2004, The Astrophysical Journal Supplement Series, 154(1), 184.
Suhasaria, T., Baratta, G. A., Ioppolo, S., Zacharias, H., & Palumbo, M. E., 2017, A&A, 608, A12.
Tanabashi, M., Hagiwara, K., Hikasa, K., Nakamura, K., Sumino, Y., Takahashi, F., ... & Quadt, A. (2018). Review of particle physics. Physical Review D, 98(3), 030001.
Thi, W. F., van Dishoeck, E. F., Dartois, E., Pontoppidan, K. M., Schutte, W. A., Ehrenfreund, P., ... & Fraser, H. J., 2006, A&A, 449(1), 251-265.
Tielens, A. G. G. M., Tokunaga, A. T., Geballe, T. R., & Baas, F., 1991, ApJ, 381, 181-199.
Tielens, A. G. G. M., 2013, Reviews of Modern Physics, 85(3), 1021.
Trottier, A., & Brooks, R. L., 2004, ApJ, 612(2), 1214.
Watanabe, N., Mouri, O., Nagaoka, A., Chigai, T., Kouchi, A., & Pirronello, V., 2007, ApJ, 668(2), 1001.
Whittet, D. C. B., Cook, A. M., Chiar, J. E., Pendleton, Y. J., Shenoy, S. S., & Gerakines, P. A., 2009, ApJ, 695(1), 94.
Whittet, D. C. B., Shenoy, S. S., Bergin, E. A., Chiar, J. E., Gerakines, P. A., Gibb, E. L., ... & Neufeld, D. A., 2007, ApJ, 655(1), 332.
Whittet, D. C. B., Poteet, C. A., Chiar, J. E., Pagani, L., Bajaj, V. M., Horne, D., ... & Adamson, A. J., 2013, ApJ, 774(2), 102.
Ziegler, James F., M. D. Ziegler, and J. P. Biersack, 2010, NIMB 268, no. 11 (2010): 1818-1823.